Nano Research 2015, 8(11): 3512–3523
DOI 10.1007/s12274-015-0851-6
Research Article
ISSN 1998-0124
CN 11-5974/O4

Self-assemblies of plasmonic gold/layered double hydroxides with highly efficient antiviral effect against the hepatitis B virus

Gabriela Carja[1] (✉), Elena Florentina Grosu[1], Catalina Petrarean[2], and Norica Nichita[2]

[1] *Department of Chemical Engineering, Faculty of Chemical Engineering and Environmental Protection, Technical University "Gh. Asachi" of Iasi, Bd. Mangeron No. 71, Iasi 700554, Romania*

[2] *Department of Viral Glycoproteins, Institute of Biochemistry of the Romanian Academy, Splaiul Independentei 296, Bucharest 060031, Romania*

Received: 12 March 2015
Revised: 1 July 2015
Accepted: 2 July 2015

KEYWORDS

plasmonic gold,
layered double hydroxides,
layered double hydroxide (LDH),
antiviral effect,
HBV,
hepatitis,
cytotoxicity

ABSTRACT

Engineering complex nanocomposites that specifically target the hepatitis B virus (HBV) and overcome the limitations of current therapies such as limited efficacy and serious side effects is very challenging. Here, for the first time, the antiviral effect of engineered plasmonic gold and layered double hydroxide self-assemblies (AuNPs/LDHs) is demonstrated, using HBV as a model virus and hepatoma-derived HepG2.2.215 cells for viral replication, assembly, and secretion of infectious virions and subviral particles. AuNPs/LDHs were obtained by a simple, cost-effective procedure in which small AuNPs (~3.5 nm) were directly obtained and organized on the surface of larger LDH nanoparticles (~150 nm) by exploiting the capability of MgLDH, ZnLDH, and MgFeLDH to manifest their "structural memory" in the aqueous solution of $Au(O_2CCH_3)_3$. The self-assembly approach of AuNPs and LDHs was assessed by transmission electron microscopy (TEM), X-ray photoelectron spectroscopy (XPS), powder X-ray diffraction (PXRD), and UV–Vis analysis (UV–Vis). All AuNPs/LDHs tested reduced the amount of viral and subviral particles released from treated cells by up to 80% and exhibited good cytocompatibility. AuNPs/MgFeLDH showed the highest antiviral HBV response with more than 90% inhibition of HBV secretion for the whole concentration range. Preliminary studies on the mechanism of HBV inhibition reveals that in the presence of AuNPs/LDHs, HBV particles are sequestered within the treated cells. The antiviral and low cytotoxic plasmonic properties of these Au/LDH nanocomposites indicate that they hold significant potential to be tailored as novel efficient therapeutics for the treatment of hepatitis B.

Address correspondence to carja@uaic.ro

1 Introduction

Hepatitis B is a major health problem worldwide, and is associated with as many as 1 milion deaths per year due to the development of hepatocellular carcinoma, cirrosis, and other complications [1]. Hepatitis B is caused by the hepatitis B virus (HBV). HBV is a member of the Hepadanviridae family of enveloped viruses that contain a DNA genome. It is also an important human pathogen that currently affects over 2 billion people worldwide [1]. The viral DNA genome is protected by a nucleocapsid surrounded by the small (S), medium (M) and large (L) surface proteins. These proteins are able to self-assemble into empty, non-infectious subviral particles (SVP) that are secreted in vast excess over the virions, both *in vitro* and in infected patients [2]. Significant prophylaxis against HBV infection is ensured through vaccination; however, treatment of chronic patients is problematic. Current therapies, which rely on replication inhibitors and immune response stimulators exhibit limited efficacy and serious side effects during the course of administration [3]. As a consequence, the number of chronically infected patients has been alarmingly increasing over the the past few decades, demonstrating the development of more efficient antiviral agents [4]. Due to the demand for novel targets and mechanisms to eradicate HBV, the design of bioactive nanocomposites engineered to specifically target the HBV and demonstrate an efficient antiviral effect is a novel but challenging approach [5, 6]. Recent studies have demonstrated that Ag nanoparticles (AgNPs) exhibit promising cytoprotective activities towards HIV - infected T-cells and can inhibit *in vitro* production of HBV, thus reducing the amount of extracellular virions [7]. In addition, AuNPs were shown to be particularly attractive platforms in anti-cancer therapies [8, 9]. Plasmonic NPs demonstrate specific tunable photo-responsive behaviour upon illumination (e.g. surface plasmon resonance and electron storage/charging effects) and extremely low quantum yield, whereas the absorbed photon energy might be converted into heat with high efficiency [10, 11]. To date it is still challenging to combine the functionalities of plasmonic NPs in complex self-assembled nanocomposites in order to establish non-toxic and constructive interactions within sophisticated biological systems [12, 13]. It is expected that coupling plasmonic NPs and nanostructured biocompatible supports might result in a synergistic effect in their therapeutic responses leading to improved bioactivity and biospecificity [14]. One important aspect to be considered when NPs act on biological systems is their cytotoxicity. This defines the NPs ability to adversely affect the normal physiology of the cells, as well as, to directly alter the structure of the normal cells [15]. Several studies have demonstrated that the aggregation process of NPs, as well as their texture, size, and stability are particularly important factors that can induce cytotoxicity [16]. Recent advances in NP synthesis provide new tools to develop specific fabrication procedures in which the nano-texture might be controlled, and nano-dimensions are preserved by limiting the aggregation processes of NPs [17]. Other aspects still remain key-points in establishing the non-toxic effects of NPs, one of the most important being the toxicity of the organic surfactants that are used as structure-directing agents during NP synthesis. [12]. For example, AuNPs are most often synthesized by using cetyltrimethylammonium bromide (CTAB), a cationic surfactant that tightly binds to AuNPs. It has been shown that during NP-cell interactions CTAB desorbs from the surface of AuNPs and induces cytotoxic effects and ultimately cell death [18, 19]. Another important aspect that might directly influence NP interactions with biological specimens is the use of stabilizing agents to prevent nano-unit aggregation and to conserve their nano-features. For example, AuNPs used for biological applications might have coatings of capping agents such as: citric acid, polysaccharides, surfactants, proteins, or polymers [20]. The organic additives involved in fabrication, stabilization, and coatings of NPs can strongly influence their direct interactions with cellular and intracellular components, resulting in cytotoxic responses [21]. This emphasizes the need for establishing "greener procedures" for obtaining stable, non-toxic, and bioactive nanostructures. In order to address these issues, we recently established a simple experimental procedure in which small NPs might be directly obtained and stabilized on layered double hydroxide (LDH) matrices without involving any organic additives as structure-directing

or stabilizing agents [22–24]. It exploits the capability of LDHs to form NP/LDH self-assemblies while the freshly calcined LDHs recover their original layered structure in the aqueous solutions of metal salts $Me^{y+}Y^{x-}$ by manifesting its "structural memory effect" [25, 26]. More precisely, in the active environment formed during the reconstruction process by the migration of Y^{x-} from the salt aqueous solution to the clay inter-layers, the LDH also has the capability to take up Me^{y+} cations from the aqueous solution of $Me^{y+}Y^{x-}$ and stabilize them on its surface as MeNPs or Me_xO_yNPs [27]. A detailed schematic illustrating this process is shown in Fig. 1. Toxicity studies demonstrated that LDH clays had negligible cytotoxic effects during LDH-cell interactions while the influence of LDH nanoparticles on cell viability and proliferation was negligible [28, 29]. Moreover, it was demonstrated that large LDH nanoparticles (50 to 200 nm) were selectively internalized into cells through clathrin-mediated endocytosis, with enhanced permeability and retention, without manifesting toxic effects [30].

The joined bioactive functionality of LDH matrices and plasmonic NPs might be an excellent motivation for testing cytotoxicity and the antiviral effect of their self-assembly. Here, we report for the first time the antiviral properties of AuNPs/LDHs self-assemblies using HBV as a model virus and hepatoma-derived HepG2.2.215 cells that support viral replication, assembly, and secretion of infectious virions and SVP. Three specific compositions of LDH clays were considered in this study, denoted as MgLDH, ZnLDH, and MgFeLDH and both the cytotoxicity profiles and the antiviral activity of AuNPs/LDHs self-assemblies were determined using quantitative assays. AuNPs/LDHs demonstrated significant antiviral effect, thus reducing the amount of viral particles and SVP released from treated cells by up to 80%, with no cellular toxicity.

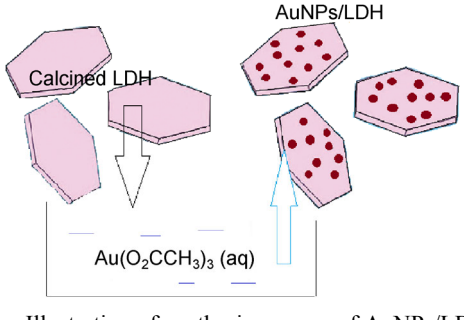

Figure 1 Illustration of synthesis process of AuNPs/LDHs self-assemblies.

2 Experimental

2.1 Preparation of LDHs

Three different LDH compositions were prepared by a co-precipitation method similar to that described by Reichle [31]. MgLDH containing Mg^{2+} and Al^{3+} (Mg^{2+}/Al^{3+} = 2/1) as cations of LDH layers was prepared by the slow addition of an aqueous solution of $Mg(NO_3)_2{\cdot}6H_2O$ and $Al(NO_3)_3{\cdot}9H_2O$, 1 M to a Na_2CO_3 (0.5×10^{-2} M) solution under stirring, at 45 °C. The pH value was kept constant at 9.5 by adding suitable amounts of 0.1 M NaOH aqueous solution. ZnLDH with Zn^{2+} and Al^{3+} in the LDH layers, (Zn^{2+}/Al^{3+} = 2/1) was obtained by slowly adding an aqueous solution of $Zn(NO_3)_2{\cdot}6H_2O$ and $Al(NO_3)_3{\cdot}9H_2O$, 1 M, to an aqueous solution of $NaOH/Na_2CO_3$ in such a way that the final pH remained at a value of 9. For MgFeLDH Mg^{2+}, Fe^{3+}, Al^{3+} were used as cation layers in a molar ratio of $Mg^{2+}/Fe^{3+}/Al^{3+}$ = 2/0.5/0.5 using a similar procedure, based on the slow addition of an aqueous solution of $Mg(NO_3)_2{\cdot}6H_2O$ and $Al(NO_3)_3{\cdot}9H_2O$, and $Fe_2(SO_4)_3$ 1 M to a Na_2CO_3 (0.5–2 M) solution, under stirring, at 45 °C. The resulting slurries were aged about 20 h at 50 °C. The final products were recuperated by filtration, washed several times with distilled water and dried under vacuum.

2.2 Preparation of AuNPs/LDHs self-assemblies

"Freshly" calcined LDHs (1 g at 500 °C for 7 h) was added, under very vigorous stirring, at 150 mL of 0.1 M aqueous solutions of $Au(O_2CCH_3)_3$ (see Fig. 1). Samples were aged at 30 °C for 7 h, washed, centrifuged, dried under vacuum and denoted as AuNPs/LDHs, where LDHs is MgLDHs, ZnLDHs or MgFeLDH while the final pH value of the reconstruction medium was 9.1, 8.3 and 8.7, respectively.

2.3 Characterization

Transmission electron microscopy (TEM) imaging was performed on a Hitachi H900 transmission electron microscope operating at an accelerating voltage of

200 kV. X-ray photoelectron spectroscopy (XPS) spectra were recorded using a Perkin-Elmer Model 5500-MT spectrometer equipped with Mg Kα radiation (1,253.6 eV), operating at 15 kV and 20 mA. The binding energies (BE) were corrected by referencing the C1s peak to 284.8 eV. Inductively coupled plasma (ICP) analysis was also used to determine the gold content of the samples. Structural characteristics, crystallinity, and purity information were recorded by X-ray diffraction (XRD) using a Shimadzu XRD 6100 diffractometer with monochromatic light (λ = 0.1541 nm), operating at 40 kV and 30 mA over a 2θ range from 4° to 70°. UV–Vis absorption spectra were recorded on a Jasco V550 spectrophotometer with integration sphere.

2.4 Cell growth and treatment

HepG2.2.2.15 cells stably transfected with two copies of the HBV genome, were grown in RPMI 1640 medium (Euroclone) containing 10% fetal bovine serum (FBS), 50 units/mL penicillin, 50 μg/mL streptomycin, 2 mM Glutamax (Invitrogen) and 200 μg/mL of G418 (Gibco). When indicated, AuNPs/LDHs were added to the medium at different concentrations to investigate their cellular toxicity and potential antiviral properties against HBV.

2.5 Cytotoxicity assay

Cytotoxicity of AuNPs/LDHs was determined by MTS (3-(4,5-dimethylthiazol-2-yl)-5-(3-carboxymethoxyphenyl)-2-(4-sulfophenyl)-2H-tetrazolium) assay, using the CellTiter 96® AQueous One Solution Cell Proliferation Assay kit (Promega, Madison, WI, USA). HepG2.2.2.15 cells were treated with serial dilutions of NPs for 3 days, before addition of the MTS reagent. Absorbance was measured at 550 nm using a microplate reader (Mitras Berthold), and expressed as the percentage of untreated (control) cells.

2.6 Quantification of HBV secretion by real-time PCR

HepG2.2.2.15 cells were grown in the absence (control) or presence of AuNPs/LDHs for 3 days. Encapsidated viral DNA was purified from cell supernatant by phenol-chloroform extraction as described [32]. The DNA was quantified by real-time PCR using the Corbett Rotor Gene 6000 system and the Maxima SYBR Green qPCR Master Mix (Fermentas). Primers were designed to amplify a 279 bp HBV-specific fragment within the S gene: HBV3575-3854_for, 5′-TCCAGGATCCTCAACAACCAGCACG-3′ and HBV3575-3854_rev, 5′-TGGCCCCCAATACCACATCATCC-3′. The number of viral genome equivalents was determined using a calibration curve containing known amounts of HBV DNA and expressed as percentages from control (untreated) samples.

2.7 Quantification of HBV SVP secretion by ELISA

The HepG2.2.2.15 supernatants used for HBV quantification were also analyzed for the amount of secreted SVP, using the Monolisa HBsAg Ultra Kit (Bio-Rad) and a Mitras Berthold microplate reader. The results were obtained as ratios of signal to cut-off value and were converted to percentages from control (untreated) sample.

2.8 Quantification of intracellular HBV transcripts by reverse-transcription (RT) real-time PCR.

Total RNA from control or AuNPs/LDHs-treated HepG2.2.2.15 cells was isolated using Trizol (Invitrogen), and quantified using the NanoDrop2000 spectrophotometer (Thermo). Equal amounts of RNA were reverse-transcribed using the SuperScript III First-Strand Synthesis kit (Invitrogen) and HBV-specific DNA was further quantified by real-time PCR, as described above. Actin amplification was employed as an internal control. Since the primers used for the HBV amplification are specific for the S gene, the pregenomic (pg) RNA, which overlaps the entire coding region of the viral genome, was also quantified using this assay, in addition to the envelope protein transcripts.

2.9 Quantification of intracellular HBV nucleocapsid DNA

HepG2.2.2.15 cells were grown in the absence (control) or presence of AuNPs/LDHs for 3 days. Cells were counted under the microscope and equal numbers were lysed in a buffer containing 1 M Tris-HCl (pH 8), 250 mM EDTA, and 0.5% NP-40. Encapsidated viral DNA was further purified from cell lysates by phenol-

chloroform extraction and quantified by real-time PCR as described above.

2.10 Quantification of intracellular HBV envelope proteins by sodium-dodecyl sulfate-polyacrylamide gel electrophoresis (SDS-PAGE) and Western blot

AuNPs/LDHs-treated and control HepG2.2.2.15 cells were lysed in a buffer containing 10 mM Tris-HCl (pH 7.5), 150 mM NaCl, 2 mM EDTA, 0.5% TritonX-100, and a mixture of protease inhibitors (Sigma-Aldrich). Cell lysates were centrifuged at 14,000 x *g* for 10 min and the total protein content was determined in clear supernatants using the BCA method (Pierce). Equal amounts of proteins were loaded for SDS-PAGE and transferred to nitrocellulose membranes using a semi-dry blotter (BioRad). The HBV proteins were detected by Western blot following successive incubations of the membrane with mouse anti-PreS1 (Santa Cruz, dilution 1:1,000) and HRP-labelled rabbit anti-mouse antibodies (Santa Cruz, dilution 1:10,000). The proteins were visualized using the ECL detection system (GE Healthcare).

3 Results and discussion

3.1 Physical-chemical characteristics of AuNPs/LDHs self-assemblies

The morphology and microstructure of AuNPs/LDHs assemblies were assessed by TEM and high-resolution TEM (HRTEM) (Fig. 2). A representative TEM image is shown in Fig. 2(a), and the presence of aggregates of large and thin platelets with a mean diameter of about 150 nm was observed. This morphology is consistent with that reported for LDH-like crystallites [33, 34], and is almost similar for all AuNPs/LDHs. In magnified images, very small nanoparticles could be easily observed as dark contrast dots, which were well-dispersed, not only over the surface (Fig. 2(b)) but also at the interfaces (Fig. 2(d)) of the LDH particles. The small NPs were almost spherical as shape and their average size, obtained by statistical analysis, was determined to be 3.2, 3.7, and 2.9 nm, for AuNPs/MgLDH, AuNPs/MgFeLDH and AuNPs/ZnLDH, respectively (Table 1). No evidence of small NPs unattached to the LDHs was found confirming these

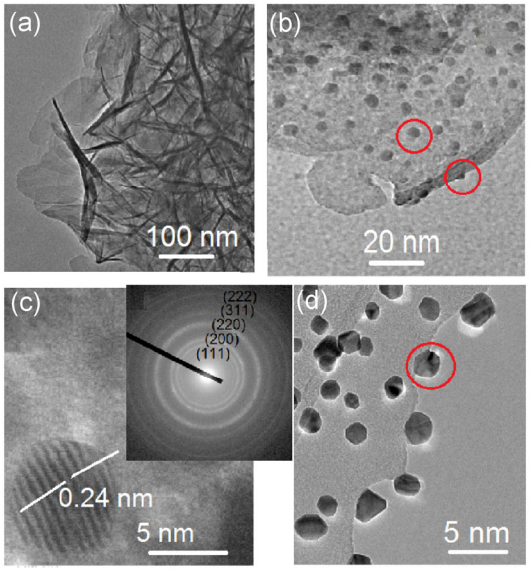

Figure 2 TEM image of (a) AuNPs/MgLDH, and (b) AuNPs/ZnLDH. (c) HRTEM image of AuNPs/MgFeLDH and (d) AuNPs/MgLDH.

Table 1 Physical-chemical characteristics of AuNPs/LDHs self-assemblies

AuNPs/LDHs	D_{Au} (nm)	XPS	ICP
		Au (at.%)	
AuNPs/MgLDH	3.2	3.7	4.0
AuNPs/ZnLDH	2.9	3.7	3.9
AuNPs/MgFeLDH	3.7	4.0	4.1

were formed and stabilized only on the surface of the LDHs. The lattice fringes with an interplanar spacing of 0.24 nm are observed and assigned to the {111} planes of face-centered cubic (fcc) Au (JCPDS No. 04-0784) (Fig. 2(c)), which confirmed the crystalline character of the small NPs. Furthermore, the selected area electron diffraction (SAED) pattern in the inset of Fig. 2(c) reveals a set of bright concentric rings in which the diffractions from (111), (200), (220), (311), and (222) planes of fcc gold can be indexed [35, 36]. Therefore, the small NPs represented as dark dots dispersed on the particles of LDHs might be identified as NPs of Au.

XPS results further confirmed the formation of AuNPs/LDHs assemblies and highlighted their similar Au content (equal to ~4%, as indicated in Table 1). For AuNPs/MgFeLDH, the survey XPS spectra is presented in Fig. 3 while the XPS spectra of AuNPs/MgLDHs

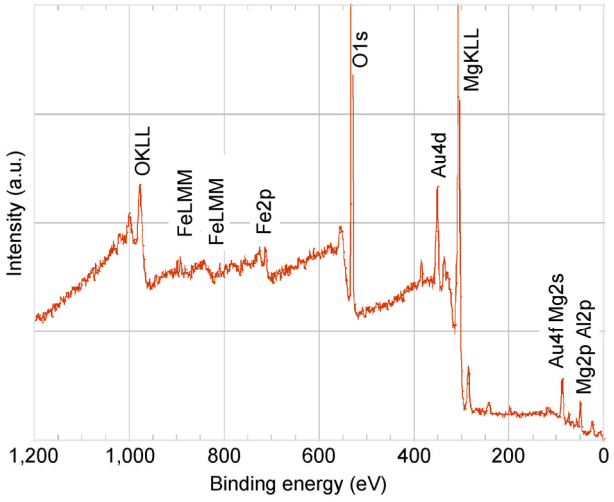

Figure 3 The survey XPS spectrum of AuNPs/MgFeLDH.

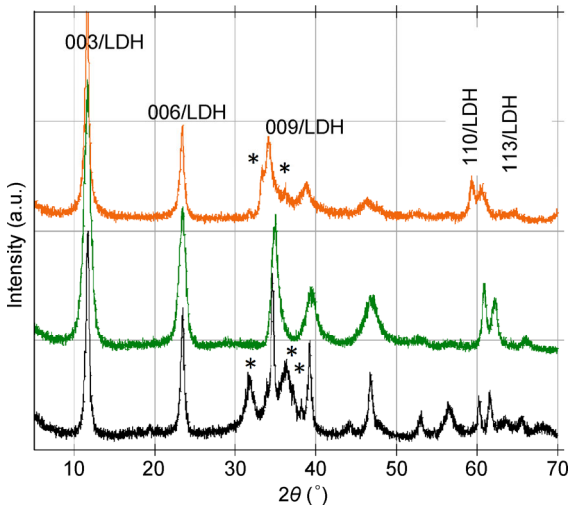

Figure 4 XRD patterns of AuNPs/ZnLDH; AuNPs/MgLDH; AuNPs/MgFeLDH.

and AuNPs/ZnLDHs are shown in Fig. S1 (in the Electronic Supplementary Material (ESM)).

The XPS analysis detected peaks from Au, Mg, Fe, Al, and O for AuNPs/MgFeLDH while Au, Zn, Al, and O were identified in the surface elemental composition of AuNPs/ZnLDH. For AuNPs/MgLDH, Au, Mg, Al, and O were identified from the binding energy (BE) values of Au4f, Mg2p, Al2p, and O1s. These results indicate the joined surface composition of AuNPs and specific LDH clay matrix. The phase identity of the AuNPs/LDHs was further confirmed by XRD analysis. The XRD patterns are depicted in Fig. 4. For AuNPs/MgLDH, the X-ray diffraction pattern demonstrated the presence of a single crystalline phase with reflections clearly assigned to the regular layered structure of hydrotalcite-like clay (ICDD file No. 22-700), in which a series of sharp and symmetric basal reflections of the (00ℓ, ℓ = 3, 6, 9) planes and broad, less intense, reflections for the nonbasal (01ℓ, ℓ = 2, 5, 8) planes were easily recognized [34, 37]. However, the XRD patterns of AuNPs/ZnLDH and AuNPs/MgFeLDH demonstrated that in addition to the reflections assigned to the regular layered structure of LDH some weaker reflections (marked by (*) in Fig. 4), with positions that roughly coincide with those of mixed oxides that define the structure of the calcined LDHs, were also present.

This indicates that the reconstruction process of the LDHs was complete for AuNPs/MgLDH but not for AuNPs/ZnLDH and AuNPs/MgFeLDH. We also observed that all (00l) reflections were characterized by high intensities, demonstrating the high crystallinity of the reconstructed LDH-like phase. The LDHs average crystallite sizes were calculated from the (003) and (006) reflections using the Debye-Scherrer equation [38]. The obtained values are around 150 nm, and are consistent with that given by TEM analysis. The interlayer space (where 0.48 nm is the width of the brucite-like layer) was calculated as 1.24 ± 0.1 nm, assuming a 3R stacking of the layers and from the positions of the peaks due to the planes (003) and (110). The value is the consequence of the expanded LDHs layers, due to the intercalation of acetate anions into the inter-layer spaces of the reconstructed LDHs, which is consistent with that previously reported by Prevot et al. [39] for acetate intercalated LDHs. No peak characteristic of the Au phase was observed in the patterns of AuNPs/LDHs, although it should be noted that such small and highly dispersed NPs might not be detectable by XRD analysis [40]. In a previous study, we showed that calcination at high temperatures of NPs/LDHs self-assemblies gives rise to a high increase (up to ten times) in the size of the supported NPs due to their aggregation process [23]. As a consequence, after calcination, the larger NPs could be detected by XRD analysis [22, 23]. Therefore, we further analyzed the XRD patterns of the AuNPs/LDHs calcined at 750 ˚C (Fig. 5).

This demonstrates that the layered LDH structure was destroyed giving rise to mixed oxides, with compositions determined by the specific compositions of

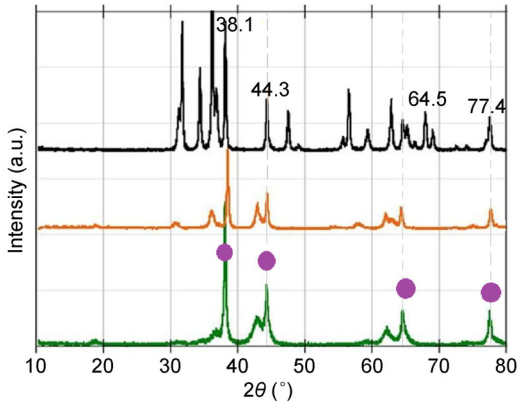

Figure 5 The XRD patterns of ▌AuNPs/ZnLDH; ▌AuNPs/MgLDH; ▌AuNPs/MgFeLDH after calcination at 750 ˚C.

their LDH precursors. Furthermore, the XRD spectra of the calcined samples show some common reflections defined by four well developed reflections at 2θ = 38.1°, 44.3°, 64.5° and 77.4° that matched to the diffraction lines of the (111), (200), (220) and (311) planes of fcc of Au (JCPDS Card No. 65-2870). The peak corresponding to the (111) plane is more intense than the other planes, suggesting that (111) is the predominant orientation. The identification of the crystalline Au by XRD analysis, after calcination at 750 ˚C, is due to the increase in the size of AuNPs during the calcination process. Figure 6 compares the UV–Vis spectra of AuNPs/LDHs. As expected from the change in color of AuNPs/LDHs (the inset of Fig. 6) the strong and broad surface plasmon resonance (SPR) band, a marker of well-dispersed AuNPs [41], was clearly observed in all AuNPs/LDHs.

This provides strong evidence for the presence of nanosized-Au in AuNPs/LDHs assemblies. For all samples, absorption in the UV region was defined by high intensity peaks, which were assigned to the optical responses of the LDH matrices and/or their derived mixed oxides, under conditions in which the structural reconstruction processes of ZnLDH and MgFeLDH were not complete, as determined by the XRD results. Apart from the absorption in the UV region, the SPR band of AuNPs can be clearly identified by a peak centered at 535 nm. This value indicates the presence of the gold in its metallic state [42]. Hence, this confirms that the state of AuNPs was not influenced by the different composition of the LDHs. However, the SPR peak intensity increased

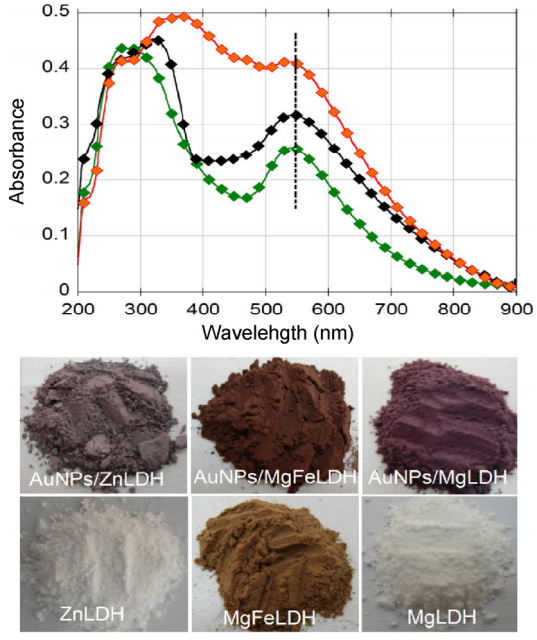

Figure 6 UV–Vis absorption spectra of ▌AuNPs/ZnLDH; ▌AuNPs/MgLDH; ▌AuNPs/MgFeLDH.

from AuNPs/MgLDH to AuNPs/ZnLDH and AuNPs/MgFeLDH without any shift in the position. It is known that the intensity of the plasmon absorbance might be influenced by the gold content, the particle size of gold, or the nano-gold surroundings environment [43, 44]. Considering that AuNPs/LDHs are defined by the similar gold content and AuNP dimensions in Table 1, the different compositions of the LDHs might provide specific environmental characteristics for AuNPs in gold-clay assemblies [23]. Thus, the specific environment of the clay matrix might give rise to the specific features of the plasmonic responses of AuNPs in AuNPs/LDHs assemblies.

3.2 Cytotoxicity of AuNPs/LDHs

The cytotoxicity of AuNPs/LDHs assemblies was evaluated to rule out any interference with potential antiviral effects. The viability of HepG2.215 cells was determined relative to control, as a function of the different AuNPs/LDHs concentrations (15, 30, 60, 125 and 250 μg/mL) after 3 days of incubation (Fig. 7). The results show that the cells exposed to AuNPs/MgFeLDH were greater than 94% viable regardless of the concentration used (Fig. 7(a)). Incubation with AuNPs/ZnLDH resulted in no significant loss of viability for concentrations up to 125 μg/mL. However,

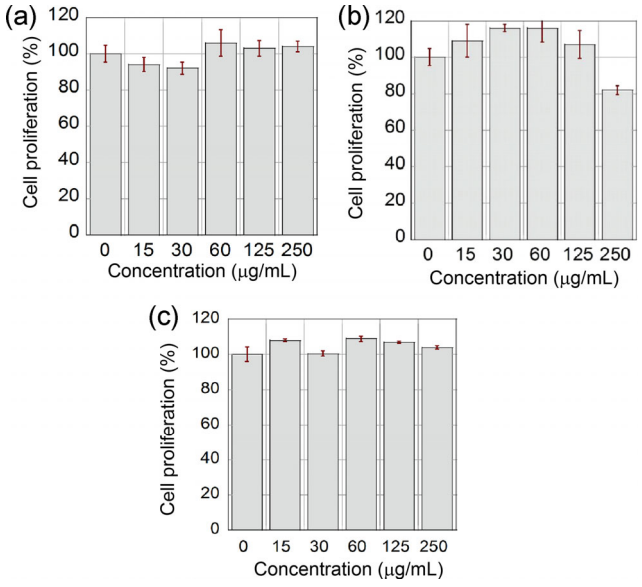

Figure 7 Cytotoxicity data for (a) AuNPs/MgFeLDH; (b) AuNPs/ZnLDH; (c) AuNPs/MgLDH.

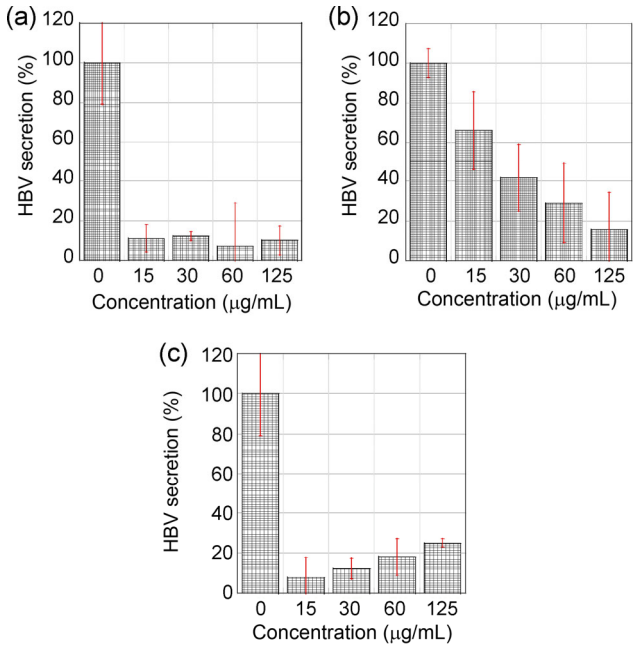

Figure 8 Inhibitory effect of (a) AuNPs/MgFeLDH; (b) AuNPs/ZnLDH; (c) AuNPs/MgLDH on the expression of the hepatitis B virus.

when the AuNPs/ZnLDHs concentration was increased to 250 μg/mL the cell viability lowered by almost 20% (Fig. 7(b)). Furthermore, AuNPs/MgLDH were completely non-toxic to cells at all concentrations tested (Fig. 7(c)).

Based on these results we considered a non-toxic concentration range of 0–125 μg/mL for all samples in further investigations of their effect against HBV.

3.3 Antiviral activity of AuNPs/LDHs

To evaluate the ability of AuNPs/LDH to inhibit HBV, the virus particles load was quantified in supernatants of HepG2.2.2.15 cells treated with a range of NPs concentrations. Remarkably, all AuNPs/LDH formulations demonstrated a significant antiviral effect (Fig. 8) AuNPs/MgFeLDH were the most potent (more than 90% inhibition of HBV secretion) (Fig. 8(a)). While AuNPs/ZnLDH inhibited HBV in a dose-dependent manner (Fig. 8(b)), a peculiar pattern was observed for AuNPs/MgFeLDH, which was already very efficient at low concentrations (Fig. 8(a)). A similar effect was evidenced for AuNPs/MgLDH, which appeared to lose some antiviral potency with increasing concentrations (Fig. 8(c)).

Considering the similar nano-gold content in AuNPs/LDHs, the specific antiviral behavior might be a consequence of the particular kinetic features of intracellular Au release from AuNPs/LDHs assemblies, which could be a function of the different composition of the LDHs. Thus, we might assume that this process is more efficient for the AuNPs/MgFeLDH and AuNPs/MgLDH, rather than for the AuNPs/ZnLDH. This hypothesis supposes that the threshold required for the Au-induced HBV inhibition is rather low. Interestingly, unlike the AuNPs/MgLDH, the other two AuNPs formulations did not significantly inhibit the secretion of non-infectious HBV particles (Fig. 9, panels (a) and (b)). This suggests that the effect observed in Fig. 8 is virus-specific, and AuNPs/LDHs nanostructured assemblies do not impair the conventional cell secretory pathway [45].

In contrast, the AuNPs/MgLDH inhibition of both viral and subviral HBV particles (Figs. 8 and 9(c)), might indicate an interference with either their assembly or secretion. It is interesting to note that a previous report has shown little efficacy of 10 nm gold nanoparticles prepared by sodium citrate reduction, against HBV [46]. These differences in HBV inhibition cannot be accounted for by the size and shape of NPs, as the AuNPs introduced here are also very small, ranging between 2.9 and 3.7 nm. Rather, the environment provided by the clay matrix structure, possibly enabling

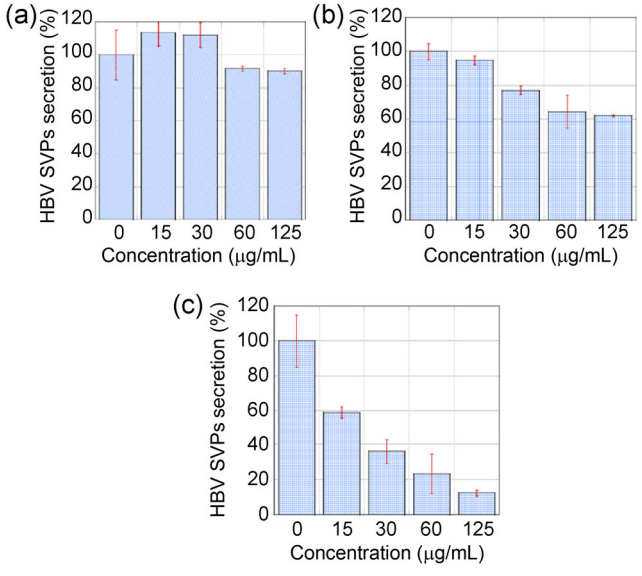

Figure 9 Inhibitory effect of (a) AuNPs/MgFeLDH; (b) AuNPs/ZnLDH; (c) AuNPs/MgLDH on the expression of SVP.

controlled release of nano-gold and preventing premature aggregation of NPs, might be the key factor of the improved antiviral properties of these assemblies. Furthermore, the results demonsreated that all the as-synthesized LDHs showed a modest antiviral activity of about 20% inhibition of HBV (see Fig. S2 in the ESM). It is also important to note that the cellular toxicity of AuNPs/LDHs nanostructured assemblies is significantly lower than that of the LDH matrices (Fig. S3 in the ESM), revealing a cell protective effect induced by the presence of nano-gold.

3.4 The mechanism of AuNPs/LDHs action against HBV

The HBV life-cycle begins with virion attachment to specific receptors at the hepatocyte surface, removal of the envelope within the endocytic pathway, and the release of the circular, partially double stranded DNA (pdsDNA) genome from the naked nucleocapsid [47]. The hepatocyte nucleus hosts the pdsDNA convertion into covalently closed circular DNA (cccDNA), which serves as a template for transcription of pregenomic (pg) and subgenomic mRNAs. These are exported to the cytoplasm where the pgRNA is reverse-transcribed into pdsDNA within the viral nucleocapsid [47]. The HepG2.2.2.15 cells were stably transfected with two copies of the HBV genome and allowed to replicate for a full replication cycle, assembly, and secretion of SVPs and infectious virions. However, they are not susceptible to infection and no horizontal spreading of the virus occured in these cells (or in other *in vitro* cellular models). Therefore, to elucidate the mechanism of HBV inhibition, we investigated the important steps of viral replication/assembly and protein synthesis in the presence of the highest AuNPs/LDHs concentration (125 μg/mL), which efficiently reduced the virus load. Quantification of the HBV transcripts showed no significant changes between control and treated cells (Fig. 10(a)), indicating that neither viral transcription nor RNA stability were affected by AuNPs/LDHs. Next, the synthesis of HBV DNA was investigated in intact nucleocapsids extracted form control and AuNPs/LDHs-treated cells. Surprisingly, the amount of viral DNA was significantly higher in the presence of AuNPs/LDHs (Fig. 10(b)).

In correlation with the drastic reduction of the virus particles in cell supernatants (Fig. 8), this result strongly suggests that the HBV particles are sequestered within treated cells. This hypothesis is also supported by the

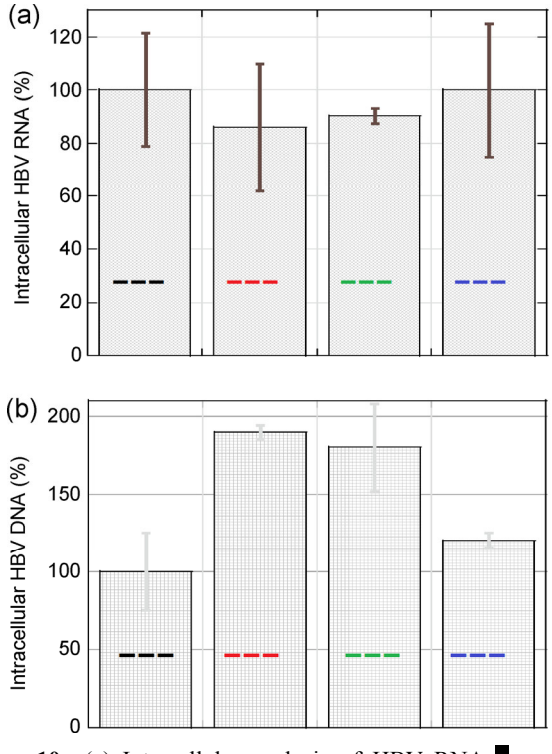

Figure 10 (a) Intracellular analysis of HBV RNA ■ control; ■ AuNPs/MgFeLDH; ■ AuNPs/ZnLDH; ■ AuNPs/MgLDH. (b) Intracellular analysis of HBV DNA ■ control; ■ AuNPs/MgFeLDH; ■ AuNPs/ZnLDH; ■ AuNPs/MgLDH; for a AuNPs/LDHs concentration of 125 μg/mL.

analysis of the L envelope protein, which plays crucial roles in nucleocapsid envelopment, while being less incorporated in SVPs. Similar to the observed effect on viral DNA, the AuNPs/LDHs induced a clear accumulation of both, glycosylated (gp) and non-glycosylated (p) L isoforms (Fig. 11). Since the level of viral mRNAs was similar in control and treated cells, the effect observed indicates a strong intracellular retention of these proteins in the presence of AuNPs/LDHs.

These interesting effects suggest a direct interaction between viral particles and AuNPs/LDHs, leading to trapping of the former inside cells. Future studies will address the exact nature of these interactions and whether the naked nucleocapsid, enveloped particles, or even the viral DNA are involved. Inhibition of HBV secretion is a valuable mechanism of action, especially in the context of a complete HBV life cycle *in vivo*, preventing virus spreading and reinfection.

4 Conclusions

Self-assemblies of plasmonic gold and layered double hydroxides have been probed as novel potential antiviral therapeutics against hepatitis B virus. AuNPs/MgFeLDH demonstrated the highest antiviral HBV response with more than 90% inhibition of HBV secretion at very low concentrations, while for AuNPs/ZnLDH, the HBV inhibition was dose dependent. A direct interaction between viral particles and AuNPs/LDHs was observed leading to trapping of the formers inside cells. AuNPs/LDHs are similar regarding their gold content, the texture of the gold nanoparticles, therefore, the observed specific antiviral behavior might be a consequence of the specific composition of the LDHs that might establish particular features of gold release from AuNPs/LDHs composites and/or give rise to specific synergetic effects between the plasmonic gold and the particular LDHs environment. The fabrication procedure of AuNPs/LDHs is simple, and takes advantage of the capability of the LDHs to form small AuNPs (~ 3.5 nm) on the larger clay particles during the structural reconstruction of the calcined LDHs in the aqueous solution of $Au(O_2CCH_3)_3$. With respect to conventional antiviral HBV drugs, the prominent advantages of AuNPs/LDHs, such as their interesting mechanism of action and good biocompatibility, open new ways towards the development of highly efficient antiviral nanocomposites.

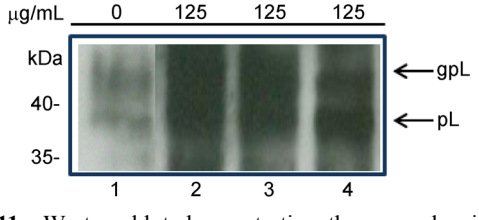

Figure 11 Western blot demonstrating the gp and p isoforms of the HBV L envelope protein in untreated, control cells (1) and cells treated with AuNPs/MgFeLDH (2), AuNPs/ZnLDH (3) or AuNPs/MgLDH (4), at the concentrations indicated. The numbers on the left represent the molecular weight of the protein in kiloDaltons (kDa).

Acknowledgments

The authors are grateful for the financial supports from the Romanian National Authority for Scientific Research, CNCS-UEFISCDI (No. PN-II-ID-PCE-75/2013) and the Romanian Academy.

Electronic Supplementary Material: Supplementary material (image characterization and supporting figures as referred to in the manuscript) is available in the online version of this article at http://dx.doi.org/10.1007/s12274-015-0851-6.

References

[1] Parkin, D. M. Global cancer statistics in the year 2000. *Lancet Oncol.* **2001**, *2*, 533–543.

[2] Huang, T. J.; Chuang, H.; Liang, Y. C.; Lin, H. H.; Horng, J. C.; Kuo, Y. C; Chen, C. W.; Tsai, F. Y.; Yen, S. C.; Chou, S. C. et al. Design, synthesis, and bioevaluation of paeonol derivatives as potential anti-HBV agents. *Eur. J. Med. Chem.* **2015**, *90*, 428–435.

[3] Yu, W. Q.; Goddard, C.; Clearfield, E.; Mills, C.; Xiao, T.; Guo, H. T.; Morrey, J. D.; Motter, N. E.; Zhao, K.; Block, T. M. et al. Design, synthesis, and biological evaluation of triazolo-pyrimidine derivatives as novel inhibitors of hepatitis B virus surface antigen (HBsAg) secretion. *J. Med. Chem.* **2011**, *54*, 5660–5670.

[4] Block, T. M.; Gish, R.; Guo, H. T.; Mehta, A.; Cuconati, A.; Thomas London, W.; Guo, J. T. Chronic hepatitis B: What should be the goal for new therapies? *Antiviral Res.* **2013**,

98, 27–34.

[5] Austin, L. A.; Mackey, M. A.; Dreaden, E. C.; El-Sayed, M. A. The optical, photothermal, and facile surface chemical properties of gold and silver nanoparticles in biodiagnostics, therapy, and drug delivery. *Arch. Toxicol.* **2014**, *88*, 1391–1417.

[6] Huang, T. J.; Chou, B. H.; Lin, C. W.; Weng, J. H.; Chou, C. H.; Yang, L. M.; Lin, S. J. Synthesis and antiviral effects of isosteviol-derived analogues against the hepatitis B virus. *Phytochemistry* **2014**, *99*, 107–114.

[7] Blecher, K.; Nasir, A.; Friedman, A. The growing role of nanotechnology in combating infectious disease. *Virulence* **2011**, *2*, 395–401.

[8] Yang, F.; Jin, C.; Subedi, S.; Lee, C. L.; Wang, Q.; Jiang, Y. J.; Li, J.; Di, Y.; Fu, D. L. Emerging inorganic nanomaterials for pancreatic cancer diagnosis and treatment. *Cancer Treat. Rev.* **2012**, *38*, 566–579.

[9] Dreaden, E. C.; El-Sayed, M. A. Detecting and destroying cancer cells in more than one way with noble metals and different confinement properties on the nanoscale. *Acc. Chem. Res*. **2012**, *45*, 1854–1865.

[10] Kennedy, L. C.; Bickford, L. R.; Lewinski, N. A.; Coughlin, A. J.; Hu, Y.; Day, E. S.; West, J. L.; Drezek, R. A. A new era for cancer treatment: Gold-nanoparticle-mediated thermal therapies. *Small* **2011**, *7*, 169–183.

[11] Luo, Y. L.; Shiao, Y. S.; Huang, Y. F. Release of photoactivatable drugs from plasmonic nanoparticles for targeted cancer therapy. *ASC Nano* **2011**, *5*, 7796–7804.

[12] Lewinski, N.; Colvin, V.; Drezek, R. Cytotoxicity of nanoparticles. *Small* **2008**, *4*, 26–49.

[13] Kostarelos, K.; Lacerda, L.; Pastorin, G.; Wu, W.; Kieckowski, S.; Luangsivilay, J.; Godefroy, S.; Pantarotto, D.; Briand, J. P.; Muller, S. et al. Cellular uptake of functionalized carbon nanotubes is independent of functional group and cell type. *Nat. Nanotechnol*. **2007**, *2*, 108–113.

[14] Thomas, M.; Klibanov, A. M. Conjugation to gold nanoparticles enhances polyethylenimine's transfer of plasmid DNA into mammalian cells. *Proc. Natl. Acad. Sci. USA.* **2003**, *100*, 9138–9143.

[15] Mackey, M. A.; Ali, M. R. K.; Austin, L. A.; Near, R. D.; El-Sayed, M. A. The most effective gold nanorod size for plasmonic photothermal therapy: Theory and *in vitro* experiments. *J. Phys. Chem. B* **2014**, *118*, 1319–1326.

[16] Mahmoud, M. A.; El-Sayed, M. A. Different plasmon sensing behavior of silver and gold nanorods. *J. Phys. Chem. Lett.* **2013**, *4*, 1541–1545.

[17] Liu, J. B.; Yu, M. X.; Zhou, C.; Zheng, J. Renal clearable inorganic nanoparticles: A new frontier of bionanotechnology. *Mater. Today* **2013**, *16*, 477–486.

[18] Goh, D.; Gong, T. X.; Dinish, U. S.; Maiti, K. K.; Fu, C. Y.; Yong, K. T.; Olivo, M. Pluronic triblock copolymer encapsulated gold nanorods as biocompatible localized plasmon resonance-enhanced scattering probes for dark-field imaging of cancer cells. *Plasmonics* **2012**, *7*, 595–601.

[19] Zhang, X. D.; Wu, H. Y.; Wu, D.; Wang, Y. Y.; Chang, J. H.; Zhai, Z. B.; Meng, A. M.; Liu, P. X.; Zhang, L. A.; Fan, F. Y. Toxicologic effects of gold nanoparticles *in vivo* by different administration routes. *Int. J. Nanomedicine*. **2010**, *5*, 771–781.

[20] Dahl, J. A.; Maddux, B. L. S.; Hutchison, J. E. Toward greener nanosynthesis. *Chem. Rev.* **2007**, *107*, 2228–2269.

[21] Hou, W.; Cronin, S. B. A review of surface plasmon resonance-enhanced photocatalysis. *Adv. Funct. Mater.* **2013**, *23*, 1612–1619.

[22] Kawamura, S.; Puscasu, M. C.; Yoshida, Y.; Izumi, Y.; Carja, G. Tailoring assemblies of plasmonic silver/gold and zinc–gallium layered double hydroxides for photocatalytic conversion of carbon dioxide using UV–visible light. *Appl. Catal. A: Gen.*, in press, DOI: 10.1016/j.apcata.2014.12.042.

[23] Carja, G.; Birsanu, M.; Okada, K.; Garcia, H. Composite plasmonic gold/layered double hydroxides and derived mixed oxides as novel photocatalysts for hydrogen generation under solar irradiation. *J. Mater. Chem. A* **2013**, *1*, 9092–9098.

[24] Seftel, E. M.; Puscasu, M. C.; Mertens, M.; Cool, P.; Carja, G. Fabrication of CeO_2/LDHs self-assemblies with enhanced photocatalytic performance: A case study on ZnSn-LDH matrix. *Appl. Catal. B: Environ*. **2015**, *164*, 251–260.

[25] Valente, J. S.; Lima, E.; Toledo-Antonio, J. A.; Cortes-Jacome, M. A.; Lartundo-Rojas, L.; Montiel, R.; Prince, J. Comprehending the thermal decomposition and reconstruction process of sol−gel MgAl layered double hydroxides. *J. Phys. Chem. C* **2010**, *114*, 2089–2099.

[26] Prince, J.; Tzompantzi, F.; Mendoza-Damián, G.; Hernández-Beltránc, F.; Valente, J. S. Photocatalytic degradation of phenol by semiconducting mixed oxides derived from Zn(Ga)Al layered double hydroxides. *Appl. Catal. B: Environ*. **2015**, *163*, 352–360.

[27] Carja, G.; Dartu, L.; Okada, K.; Fortunato, E. Nanoparticles of copper oxide on layered double hydroxides and the derived solid solutions as wide spectrum active nano-photocatalysts. *Chem. Eng. J.* **2013**, *222*, 60–66.

[28] Ariga, K.; Ji, Q. M.; McShane, M. J.; Lvov, Y. M.; Vinu, A.; Hill, J. P. Inorganic nanoarchitectonics for biological applications. *Chem. Mater.* **2012**, *24*, 728–737.

[29] Ladewig, K.; Niebert, M.; Xu, Z. P.; Gray, P. P.; Lu, G. Q. M. Efficient siRNA delivery to mammalian cells using layered double hydroxide nanoparticles. *Biomaterials* **2010**, *31*, 1821–1829.

[30] Oh, J. M.; Choi, S. J.; Lee, G. E.; Kim, J. E.; Choy, J. H.

Inorganic metal hydroxide nanoparticles for targeted cellular uptake through clathrin-mediated endocytosis. *Chem. Asian J.* **2009**, *4*, 67–73.

[31] Reichle, W. T.; Kang, S. Y.; Everhardt, D. S. The nature of the thermal decomposition of a catalytically active anionic clay mineral. *J. Catal.* **1986**, *101*, 352–359.

[32] Lazar, C.; Durantel, D.; Macovei, A.; Zitzmann, N.; Zoulim, F.; Dwek, R. A.; Branza-Nichita, N. Treatment of hepatitis B virus-infected cells with α-glucosidase inhibitors results in production of virions with altered molecular composition and infectivity. *Antiviral Res.* **2007**, *76*, 30–37.

[33] Rives, V.; del Arco, M.; Martin, C. Intercalation of drugs in layered double hydroxides and their controlled release: A review. *Appl. Clay Sci.* **2014**, *88–89*, 239–269.

[34] Rives, V. *Layered Double Hydroxides: Present and Future*; Nova Science Publishers: New York, 2011.

[35] Louis, C.; Pluchery, O. *Gold Nanoparticles for Physics, Chemistry, Biology*; Imperial College Press: London, 2012.

[36] He, J. H.; Kunitake, T. Preparation and thermal stability of gold nanoparticles in silk-templated porous filaments of titania and zirconia. *Chem. Mater.* **2004**, *16*, 2656–2661.

[37] Alanis, C.; Natividad, R.; Barrera-Diaz, C.; Martínez-Miranda, V.; Prince, J.; Valente, J. S. Photocatalytically enhanced Cr(VI) removal by mixed oxides derived from MeAl (Me: Mg and/or Zn) layered double hydroxides. *Appl. Catal. B: Environ.* **2013**, *140–141*, 546–551.

[38] Hall, B. D.; Zanchet, D.; Ugarte, D. Estimating nanoparticle size from diffraction measurements. *J. Appl. Cryst.* **2000**, *33*, 1335–1341.

[39] Prevot, V.; Briois, V.; Cellier, J.; Forano C.; Leroux, F. An *in-situ* investigation of LDH–acetate prepared in polyol, under moderate thermal treatment. *J. Phys. Chem. Solids* **2008**, *69*, 1091–1094.

[40] Horváth, A.; Beck, A.; Stefler, G.; Benkó, T.; Sáfrán, G.; Varga, Z.; Gubicza, J.; Guczi, L. Silica-supported Au nanoparticles decorated by CeO_2: Formation, morphology, and CO oxidation activity. *J. Phys. Chem. C* **2011**, *115*, 20388–20398.

[41] Kominami, H.; Tanaka, A; Hashimoto, K. Gold nanoparticles supported on cerium(IV) oxide powder for mineralization of organic acids in aqueous suspensions under irradiation of visible light of λ = 530 nm. *Appl. Catal. A: Gen.* **2011**, *397*, 121–126.

[42] Corti, C.; Holliday, R. *Gold: Science and Applications*; CRC Press: UK, 2009.

[43] Zhou, C.; Yu, J.; Qin, Y. P.; Zheng, J. Grain size effects in polycrystalline gold nanoparticles. *Nanoscale* **2012**, *4*, 4228–4233.

[44] Mignani, A.; Ballarin, B.; Giorgetti, M.; Scavetta, E.; Tonelli, D.; Boanini, E.; Prevot, V.; Mousty, C.; Iadecola, A. Heterostructure of Au nanoparticles-NiAl layered double hydroxide: Electrosynthesis, characterization, and electrocatalytic properties. *J. Phys Chem. C* **2013**, *117*, 16221–16230.

[45] Patient, R.; Hourioux, C.; Roingeard, P. Morphogenesis of hepatitis B virus and its subviral envelope particles. *Cell. Microbiol.* **2009**, *11*, 1561–1570.

[46] Lu, L.; Sun, R. W.; Chen, R.; Hui, C. K.; Ho, C. M.; Luk, J. M.; Lau G. K. K.; Che, C. M. Silver nanoparticles inhibit hepatitis B virus replication. *Antivir. Ther.* **2008**, *13*, 253–262.

[47] Bruss, V. Hepatitis B virus morphogenesis. *World J. Gastroenterol.* **2007**, *13*, 65–73.